Available online at www.sciencedirect.com
SCIENCE DIRECT®
Journal of Sound and Vibration 271 (2004) 937–957
JOURNAL OF SOUND AND VIBRATION
www.elsevier.com/locate/jsvi

The influence of a rail embankment on the vibrations generated by moving trains

A. Ditzel, G.C. Herman*

Delft University of Technology, Centre for Technical Geoscience, Mekelweg 4, 2628 CD Delft, The Netherlands

Received 15 July 2002; accepted 12 March 2003

Abstract

High-speed trains can generate strong vibrations that propagate away from the track. In this paper, an efficient method is presented to calculate the displacements generated by a train moving over an embankment. It is based on a domain-type integral equation which is solved numerically with the use of slowness-domain techniques. By expressing the field in terms of reflection and transmission properties of the layers, the effects of stratification of the embedding medium are taken into account. The results are compared to actual measurements and agree qualitatively.

1. Introduction

Intensive ground vibrations can be generated by high-speed trains and can cause annoyance to the public living or working in the vicinity of the track. Particularly in soft-soil regions, where the train speed may approach or even exceed the surface-wave speed, a high vibration level can occur. In recent years, the generation of vibrations due to high-speed trains has received considerable attention. Several methods have been developed to predict the vibrations generated by trains moving over an embankment.

Krylov [1] investigated the effect of track dynamics on the vibrations due to high-speed trains. The vibrations generated by the bending track were computed with the aid of a Green's function formulation and its far-field asymptotic behaviour in an elastic half-space. For trains travelling at a lower speed than the Rayleigh wave in the half-space, the presence of sleepers appeared to be essential for the generation of vibrations. An increased effect on the level of ground vibration occured for trains travelling at trans-Rayleigh speed.

*Corresponding author. Tel.: +31-15-2783825.
E-mail addresses: a.ditzel@math.tudelft.nl (A. Ditzel), g.c.herman@math.tudelft.nl, g.c.herman@ewi.tudelft.nl (G.C. Herman).

0022-460X/$ - see front matter
doi:10.1016/S0022-460X(03)00772-7

Sheng et al. [2,3] investigated the vibrations of a harmonic load moving over a layered ground. The track, including rails, rail pads, sleepers and ballast, was modelled by means of a multi-component mass–spring system. The ground was modelled as a structure of three-dimensional viscoelastic layers overlying either a half-space or a rigid foundation. From several calculations, it was shown that propagating waves were produced for loads travelling with a velocity higher than the critical wave speed. It was shown that both constant and harmonic loads contribute significantly to the vibrations generated by the train.

In Suiker et al. [4], the track has been modelled by means of a Timoshenko beam, laying over a half-space. Both subcritical and supercritical train speeds were investigated. It was found that the response of the system was greatly amplified when a critical state was reached, and that it is depends on the stiffness of the model. They concluded that when a railway track consists of soft-soil bases, the dynamic amplifications may cause unstable vehicle behaviour.

Metrikine and Popp [5] have investigated the vibrations of a periodically supported beam on an elastic half-space under the influence of a uniformly moving harmonically varying load. The half-space was replaced by a set of springs placed under the support of the beam. By using the equivalent stiffness of these springs it was found that the displacements depended on the frequency of the beam vibrations and on the phase shift of neighbouring supports. Moreover, it was found that a load moving with the Rayleigh wave speed caused a resonance in the system.

In the present paper, the influence of a rail embankment is investigated, where the embankment is embedded in the layered half-space. The model is an extension of the model previously presented by the authors in Ditzel et al. [6], where the response of a layered half-space to a moving (high-speed) train was investigated. In that approach, the train was modelled by means of a vertical, oscillating point source, moving over a horizontally layered, three-dimensional elastic half-space with a traction-free surface. By considering the moving source as a superposition of point forces, the wave field could be efficiently calculated in the slowness domain.

This model is extended here by including an embankment into the geometry. The mass density of the embankment differs from the density of the surrounding medium, and, as a consequence, both compressional and shear wave velocities are different. The scattering problem for a stationary source can then be formulated in terms of a domain-integral equation. Due to linearity of the resulting problem, it remains possible to apply the superposition principle and take full advantage of the efficient way of formulating the vibration problem for the moving source in terms of plane waves.

The numerical results have been compared with experimental data. The results come from a multi-receiver field experiment, consisting of three lines with three component or vertical geophones. Receivers have been placed both near to and far from the railway track, in order to measure the transfer of waves into the surrounding medium. Several train passages have been recorded and some are presented in this paper.

2. Formulation of the problem

In this section, the mathematical model is discussed. A notation similar to the one presented in Ditzel et al. [6] is used. First, the equations for wave propagation in the embedding medium are described briefly, then a description of a moving source follows and, finally, the formulation of the

domain-integral equation is given. For a more detailed description of the modelling of the embedding medium and force, the reader is referred to Ref. [6].

2.1. The layered embedding

The train is modelled as a point force which moves over an embankment, embedded in a semi-infinite elastic medium. This medium consists of N homogeneous and horizontal layers overlying a homogeneous elastic half-space. Fig. 1 shows a schematic model of a one-layer geometry. Each of the media is characterized by its density ρ_n and by its compressional and shear wave velocities α_n and β_n, with n indicating the layer number ($n = 1, N+1$). The wave velocities are assumed to be complex (with $\mathrm{Re}\{\alpha_n\} \geqslant 0$ and $\mathrm{Im}\{\alpha_n\} \leqslant 0$ and similarly for β_n) in order to take dissipation into account. A traction-free boundary condition is imposed at the surface of the medium and the radiation condition is imposed in the underlying half-space.

For each of the N layers, the elastic state is characterized by the following two equations:

$$\partial_i \tau_{ij}(\mathbf{x}) + \omega^2 \rho_n u_j(\mathbf{x}) = -f_j(\mathbf{x}), \tag{1}$$

$$\tau_{ij}(\mathbf{x}) - \lambda_n \delta_{ij} \partial_k u_k(\mathbf{x}) - 2\mu_n \partial_i u_j(\mathbf{x}) = 0 \quad \text{for } n = 1, N+1, \tag{2}$$

with u_j being the displacement and τ_{ij} the stress tensor. Furthermore, $\mathbf{x}$ is a position vector, given by $\mathbf{x} = x\mathbf{i}_1 + y\mathbf{i}_2 + z\mathbf{i}_3$ and ω is the angular frequency of the Fourier transform. In Eq. (1), f_j is the force to model the train, which moves with a constant velocity c in the x direction. In Eq. (2), λ_n

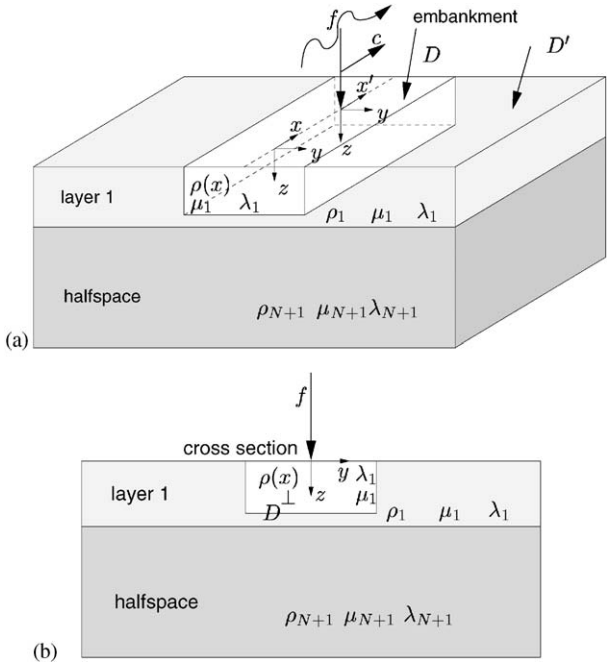

Fig. 1. (a) Geometry of the problem. The train is modelled as an oscillating force, moving with constant speed over an embankment D. The rail embankment is embedded in a horizontally layered medium. (b) Cross-section of the geometry.

and μ_n are Lamé coefficients. In the previous and following equations, the summation convention is followed for the lower indices, except for those indicating layer numbering for the soil parameters.

2.2. Moving sources

Fig. 1 shows two reference frames, one is stationary with respect to the ground, given by the co-ordinates $\mathbf{x}$, and one co-moving with the train, given by $\mathbf{x}'$. Eqs. (1) and (2) are given with respect to the stationary reference frame. In order to study the wave field generated by a moving train, a relation between the forces observed in the train and the forces observed in the ground has to be found. In Ref. [6], the authors have shown that the moving train is actually a moving point source, which can be represented by a superposition of stationary point sources, having appropriate phases. The following equation was found for the force in the frame of reference which is stationary with respect to the ground

$$f_j(\mathbf{x}) = \frac{1}{c}\int_{x_s} \mathrm{d}x_s \bar{f}_j(\mathbf{x}-\mathbf{x}_s)\mathrm{e}^{\mathrm{j}(\omega/c)x_s}\cos\left(\frac{\omega_c}{c}x_s\right), \tag{3}$$

where $f_j(\mathbf{x})$ is the moving source in the stationary reference frame, and $\bar{f}_j(\mathbf{x}-\mathbf{x}_s) = a_j\delta(\mathbf{x}-\mathbf{x}_s)$ a point source, exerted at position $\mathbf{x}_s = (x_s, 0, 0)$, and having strength a_j. The oscillatory behaviour of the train, caused by irregularities in the track and the wheels, is represented by the resonance frequency ω_c. For convenience, the ω-dependence of f_j has been omitted.

By using a complex notation for the cosine term in Eq. (3), the source term in the stationary frame of reference can be written as the sum of two terms

$$f_j(\mathbf{x}) = \tfrac{1}{2}(f_j{}^{+}(\mathbf{x}) + f_j^{-}(\mathbf{x})), \tag{4}$$

where

$$f_j^{\pm}(\mathbf{x}) = \frac{1}{c}\int_{x_s} \mathrm{d}x_s \bar{f}_j(\mathbf{x}-\mathbf{x}_s)\mathrm{e}^{\mathrm{j}[(\omega\pm\omega_c)/c]x_s}. \tag{5}$$

Similarly, the wave field u_j, generated by the moving source f_j, can also be expressed as the sum of two wave fields:

$$u_j(\mathbf{x}) = \tfrac{1}{2}(u_j^{+}(\mathbf{x}) + u_j^{-}(\mathbf{x})). \tag{6}$$

The wave fields $u_j^{\pm}$ are generated by the forces $f_j^{\pm}$, respectively, and can be obtained by superposition of wave fields $\bar{u}_j$:

$$u_j^{\pm}(\mathbf{x}) = \frac{1}{c}\int_{x_s} \mathrm{d}x_s \bar{u}_j(\mathbf{x}-\mathbf{x}_s)\mathrm{e}^{\mathrm{j}[(\omega\pm\omega_c)/c]x_s}, \tag{7}$$

where $\bar{u}_j$ is the wave field generated by a stationary point force $\bar{f}_j$. The omega dependence of $\bar{u}_j$ and u_j has been omitted for convenience.

Eq. (7) is rewritten as follows:

$$u_j^{\pm}(\mathbf{x}) = \frac{1}{c}\int_{x_s} \mathrm{d}x_s \bar{u}_j(x - x_s, y, z)\mathrm{e}^{\,\mathrm{j}\omega p_1^{\pm} x_s} \tag{8}$$

$$= \frac{1}{c}\mathrm{e}^{\,\mathrm{j}\omega p_1^{\pm} x}\int_{\tilde{x}} \mathrm{d}\tilde{x}\bar{u}_j(\tilde{x}, y, z)\mathrm{e}^{-\mathrm{j}\omega p_1^{\pm}\tilde{x}} \quad \text{with } \tilde{x} = x - x_s, \tag{9}$$

where $p_1^{\pm} = (1 \pm \omega_c/\omega)/c$. The integral in the last equation can be seen as a forward slowness transform from the (x, y, z) domain (i.e., the spatial domain) to the (p_1, y, z) domain (i.e., the slowness-space domain). Thus, the displacement reads

$$u_j^{\pm}(\mathbf{x}) = \frac{1}{c}\mathrm{e}^{\,\mathrm{j}\omega p_1^{\pm} x}\tilde{u}_j(p_1^{\pm}, y, z), \tag{10}$$

where $\tilde{u}_j(p_1^{\pm}, y, z)$ is the slowness transform in the x direction of $\bar{u}_j(x, y, z)$, the wave field for a stationary force.

2.3. Domain-integral equation formulation

In order to derive an expression for the total wave field generated by a moving force, the derivation of the wave field $\bar{u}_j$ for a non-moving source $\bar{f}_j$ is treated first. Once an expression for the wave field of a non-moving source has been found, use can be made of Eq. (7) to find the wave field u_j, generated by the moving source f_j.

In Fig. 1a, the geometry of the problem has been sketched. The embankment occupies a subdomain D of an elastic layered half-space. It is bounded in the directions perpendicular to the track and unbounded in the direction parallel to the track. Inside the embankment, the wave field $\bar{u}_j$, generated by a stationary force $\bar{f}_j$, satisfies the following equations:

$$\partial_i \bar{\tau}_{ij}(\mathbf{x}) + \omega^2 \rho(\mathbf{x})\bar{u}_j(\mathbf{x}) = -\bar{f}_j(\mathbf{x}), \tag{11}$$

$$\bar{\tau}_{ij}(\mathbf{x}) - \lambda_1 \delta_{ij}\partial_k \bar{u}_k(\mathbf{x}) - 2\mu_1 \partial_i \bar{u}_j(\mathbf{x}) = 0 \quad (\mathbf{x} \in D). \tag{12}$$

In the above equation, the stationary force $\bar{f}_j$ accounts for the interaction between the train and the rail embankment. By imposing continuity of the displacement and the stress, the interaction between the embankment and the surrounding medium is accounted for. As such, the interaction between the embankment and the embedding medium is accounted for intrinsically by the formulation of the problem. It is assumed that the Lamé parameters in the embankment, located in the top layer of the embedding medium, are the same as the parameters of this embedding layer. This simplifies the problem, but as a contrast in wave velocities between the embankment and its embedding medium can be accounted for by a density contrast, it may give a qualitative insight into the influence of the embankment on the vibration level. The basic equations for the wave field outside the embankment read

$$\partial_i \bar{\tau}_{ij}(\mathbf{x}) + \omega^2 \rho_n \bar{u}_j(\mathbf{x}) = 0, \tag{13}$$

$$\bar{\tau}_{ij}(\mathbf{x}) - \lambda_n \delta_{ij}\partial_k \bar{u}_k(\mathbf{x}) - 2\mu_n \partial_i \bar{u}_j(\mathbf{x}) = 0 \quad (\mathbf{x} \in D' \text{ and } n = 1, N+1), \tag{14}$$

where use has been made of the fact that no sources are present outside the embankment.

The wave field is considered to be made up of an incident field and a scattered field. The incident wave field $\bar{u}_j^{inc}$ is defined as the field that would be present in the absence of the embankment (i.e., if the position of the embankment were to be occupied by the same soil as in the top layer). The scattered field $\bar{u}_j^{sc}$ accounts for the embankment. Inside the embankment, the incident wave field thus satisfies the following equations:

$$\partial_i \bar{\tau}_{ij}^{inc}(\mathbf{x}) + \omega^2 \rho_1 \bar{u}_j^{inc}(\mathbf{x}) = -\bar{f}_j(\mathbf{x}), \tag{15}$$

$$\bar{\tau}_{ij}^{inc}(\mathbf{x}) - \lambda_1 \delta_{ij} \partial_k \bar{u}_k^{inc}(\mathbf{x}) - 2\mu_1 \partial_i \bar{u}_j^{inc}(\mathbf{x}) = 0 \quad (\mathbf{x} \in D), \tag{16}$$

where the embankment is located in the top layer. Therefore, the wave equations for the incident field have been set up with soil properties which are equal to those of the top layer. Outside the embankment, the incident field satisfies similar, but source-free equations:

$$\partial_i \bar{\tau}_{ij}^{inc}(\mathbf{x}) + \omega^2 \rho_n \bar{u}_j^{inc}(\mathbf{x}) = 0, \tag{17}$$

$$\bar{\tau}_{ij}^{inc}(\mathbf{x}) - \lambda_n \delta_{ij} \partial_k \bar{u}_k^{inc}(\mathbf{x}) - 2\mu_n \partial_i \bar{u}_j^{inc}(\mathbf{x}) = 0 \quad (\mathbf{x} \in D' \text{ and } n = 1, N+1). \tag{18}$$

By rewriting Eq. (11), the following system of equations for the wave field inside the embankment is obtained:

$$\partial_i \bar{\tau}_{ij}(\mathbf{x}) + \omega^2 \rho_1 \bar{u}_j(\mathbf{x}) = -\bar{f}_j(\mathbf{x}) - \omega^2 (\rho(\mathbf{x}) - \rho_1) \bar{u}_j(\mathbf{x}), \tag{19}$$

$$\bar{\tau}_{ij}(\mathbf{x}) - \lambda_1 \delta_{ij} \partial_k \bar{u}_k(\mathbf{x}) - 2\mu_1 \partial_i \bar{u}_j(\mathbf{x}) = 0 \quad (\mathbf{x} \in D). \tag{20}$$

By subsequently subtracting Eqs. (15) and (16) from Eqs. (19) and (20), the equations for the scattered wave field inside the embankment are obtained

$$\partial_i \bar{\tau}_{ij}^{sc}(\mathbf{x}) + \omega^2 \rho_1 \bar{u}_j^{sc}(\mathbf{x}) = -\omega^2 (\rho(\mathbf{x}) - \rho_1) \bar{u}_j(\mathbf{x}), \tag{21}$$

$$\bar{\tau}_{ij}^{sc}(\mathbf{x}) - \lambda_1 \delta_{ij} \partial_k \bar{u}_k^{sc}(\mathbf{x}) - 2\mu_1 \partial_i \bar{u}_j^{sc}(\mathbf{x}) = 0 \quad (\mathbf{x} \in D). \tag{22}$$

Outside the embankment, the wave equations for the scattered field are obtained by subtracting Eqs. (17) and (18) from Eqs. (13) and (14).

The incident field is generated by the volume source term $\bar{f}_j(\mathbf{x})$, whereas the scattered wave field is caused by the source term $\omega^2(\rho(\mathbf{x}) - \rho_1)\bar{u}_j(\mathbf{x})$. Now, an integral representation for the wave field generated by a stationary point source can be derived

$$\bar{u}_j(\mathbf{x}) = \bar{u}_j^{inc}(\mathbf{x}) + \int_D \mathrm{d}V(\tilde{\mathbf{x}}) \omega^2 (\rho(\tilde{y}, \tilde{z}) - \rho_1) \bar{u}_{jk}^G(\mathbf{x}; \tilde{\mathbf{x}}) \bar{u}_k(\tilde{\mathbf{x}}), \tag{23}$$

with

$$\bar{u}_j^{inc}(\mathbf{x}) = \int_D \mathrm{d}V(\tilde{\mathbf{x}}) \bar{u}_{jk}^G(\mathbf{x}; \tilde{\mathbf{x}}) \bar{f}_k(\tilde{\mathbf{x}}), \tag{24}$$

with the density contrast only depending on the co-ordinates perpendicular to the track (i.e., $\rho(x, y, z) = \rho(y, z)$). For more details, the reader is referred to Pao and Varatharajulu [7], where representations similar to Eqs. (23) and (24) can be found in somewhat different form.

In Eq. (23), $\bar{u}_{jk}^G(\mathbf{x}; \tilde{\mathbf{x}})$ represents the Green's tensor, which is the wave field generated by a non-moving point force, exerted at position $\tilde{\mathbf{x}}$ and observed at position $\mathbf{x}$. It satisfies the following

elastodynamic wave equations:

$$\partial_i \bar{\tau}^G_{ijl}(\mathbf{x};\tilde{\mathbf{x}}) + \omega^2 \rho_n \bar{u}^G_{jl}(\mathbf{x};\tilde{\mathbf{x}}) = -\delta_{jl}\delta(\mathbf{x}-\tilde{\mathbf{x}}), \tag{25}$$

$$\bar{\tau}^G_{ijl}(\mathbf{x};\tilde{\mathbf{x}}) - \lambda_n \delta_{ij}\partial_k \bar{u}^G_{kl}(\mathbf{x};\tilde{\mathbf{x}}) + 2\mu_n \partial_i \bar{u}^G_{jl}(\mathbf{x};\tilde{\mathbf{x}}) = 0 \quad (n = 1, N+1), \tag{26}$$

where $\delta(\mathbf{x}-\tilde{\mathbf{x}})$ denotes a three dimensional unit pulse, and δ_{jl} the Kronecker delta. For convenience, in Eqs. (25)–(26), the ω-dependence of $\bar{u}^G_{jl}$ has been omitted.

In Section 2.2, it has been shown that the wave field generated by a moving source can be obtained by superposition of wave fields generated by a stationary point force. Application of the same method as outlined in Eqs. (8)–(10) to Eq. (23) results in the following integral representation of the wave field in terms of slowness $p_1^{\pm}$:

$$\tilde{u}_j(p_1^{\pm}, y, z) = \tilde{u}^{inc}_j(p_1^{\pm}, y, z) + \int_{D^{\perp}} \mathrm{d}y'\mathrm{d}z' \Delta\rho(y', z')\omega^2 \times \tilde{u}^G_{jk}(p_1^{\pm}, y-y', z; z')\tilde{u}_k(p_1^{\pm}, y', z'), \tag{27}$$

with the mass density contrast given by $\Delta\rho(y', z') = \rho(y', z') - \rho_1$. The domain integration is only performed over $D^{\perp}$, a cross-section of the embankment (see Fig. 1b). In Eq. (27), $\tilde{u}_k$ and $\tilde{u}^G_{jk}$ are the slowness transforms with respect to the x co-ordinate of u_k and u^G_{jk}. For a complete derivation of this integral representation, the reader is referred to Appendix A.

In this study, the case has been treated for which there is only a difference in mass density between the embankment and the surrounding medium.

The more general case with contrasts in both density and Lamé parameters runs along similar lines but more effort is required to account for the source term in the constitutive relation. The numerical computation becomes considerably more difficult and thus more time consuming. Integral representations for this case (for a stationary source) are also given by Pao and Varatharajulu [7] and Tan [8].

2.4. Solution of the integral equation

Eq. (27) is a domain-integral equation if the observation point (y, z) is located in $D^{\perp}$. It is a Fredholm integral equation of the second type, and it can be written as follows:

$$\int_{D^{\perp}} \mathrm{d}y'\mathrm{d}z' \{\delta_{jk}\delta(y-y')\delta(z-z') - \Delta\rho(y', z')\omega^2 \tilde{u}^G_{jk}(p_1^{\pm}, y-y', z; z')\}\tilde{u}_k(p_1^{\pm}, y', z') = \tilde{u}^{inc}_j(p_1^{\pm}, y, z) \quad ((y, z) \in D^{\perp}). \tag{28}$$

This equation can be solved with the method of moments. This method consists of several steps. First, a discretization of the contrast region $D^{\perp}$ is performed. Then, an appropriate choice of expansion and weighing functions is made and finally the expansion coefficients are calculated.

The discretization of the contrast region is obtained by using a uniform square mesh with grid size δ. The expansion functions are chosen such that

$$\tilde{u}_k(p_1^{\pm}, y, z) = \sum_{p=1}^{M} \sum_{q=1}^{N} a_k^{(pq)} \phi^{(p)}(y) \phi^{(q)}(z). \tag{29}$$

The functions $\phi^{(p)}(y)$ are defined by

$$\phi^{(p)}(y) = \begin{cases} 1 & y^{(p)-} < y < y^{(p)+}, \\ 0 & \text{otherwise} \end{cases} \tag{30}$$

with $y^{(p)\pm} = y^{(p)} \pm \delta/2$. Similar forms are obtained for functions $\phi^{(q)}(z)$. Co-ordinates $(y^{(p)}, z^{(q)})$ denote the centre of the square grid cell. The weighing functions are chosen to be Dirac delta pulses

$$\xi^{(m)}(y) = \delta(y - y^{(m)}) \quad \text{and} \quad \xi^{(n)}(z) = \delta(z - z^{(n)}). \tag{31}$$

In this way, the discretized version of Eq. (28) can be written as a two-dimensional linear equation, which reads

$$\sum_{p=1}^{M} \sum_{q=1}^{N} G_{jk}^{(mn,pq)} a_k^{(pq)} = c_j^{(mn)}, \tag{32}$$

where the summation convention is understood for lower indices. In Eq. (32), matrix $G_{jk}^{(mn,pq)}$ is given by

$$\begin{aligned} G_{jk}^{(mn,pq)} &= \int\int_{y',z'} \mathrm{d}y' \mathrm{d}z' \xi^{(m)}(y') \xi^{(n)}(z') \int\int_{\tilde{y},\tilde{z}} \mathrm{d}\tilde{y}\, \mathrm{d}\tilde{z} \phi^{(p)}(\tilde{y}) \phi^{(q)}(\tilde{z}) \\ &\quad \times \{\delta(y' - \tilde{y}) \delta(z' - \tilde{z}) \delta_{jk} - \Delta\rho(\tilde{y}, \tilde{z}) \omega^2 \tilde{u}_{jk}^G(p_1, y' - \tilde{y}, z'; \tilde{z})\} \\ &= \delta_{jk} \delta_{pm} \delta_{nq} - \int_{y^{(p)-}}^{y^{(p)+}} \mathrm{d}\tilde{y} \int_{z^{(q)-}}^{z^{(q)+}} \mathrm{d}\tilde{z} \Delta\rho(\tilde{y}, \tilde{z}) \omega^2 \tilde{u}_{jk}^G(p_1, y^{(m)} - \tilde{y}, z^{(n)}; \tilde{z}). \end{aligned} \tag{33}$$

For the determination of the coefficients of matrix $G_{jk}^{(mn,pq)}$, expressions for $\tilde{u}_{jk}^G$ are needed for all combinations of source and receiver points. In a previous article by the authors [6], a method was developed for determining the tensor $\tilde{u}_{jk}^G$. The calculation is performed by transforming from the spatial y-domain to the slowness p_2-domain. The slowness transform is defined by

$$\tilde{u}_{jk}^G(p_1, y, z; z') = \frac{\omega}{2\pi} \int_{p_2} \mathrm{d}p_2 \mathrm{e}^{\mathrm{j}\omega p_2 y} \tilde{\tilde{u}}_{jk}^G(p_1, p_2, z; z'), \tag{34}$$

where $\tilde{\tilde{u}}_{jk}^G$ is the double-slowness transform of the displacement u_{jk}^G. Using this slowness representation of the Green's function, matrix $G_{jk}^{(mn,pq)}$ can be expressed as

$$\begin{aligned} G_{jk}^{(mn,pq)} &= \delta_{jk} \delta_{pm} \delta_{nq} - \int_{y^{(p)-}}^{y^{(p)+}} \mathrm{d}\tilde{y} \int_{z^{(q)-}}^{z^{(q)+}} \mathrm{d}\tilde{z} \Delta\rho(\tilde{y}, \tilde{z}) \omega^2 \\ &\quad \times \frac{\omega}{2\pi} \int_{p_2} \mathrm{d}p_2 \mathrm{e}^{\mathrm{j}\omega p_2 (y^{(m)} - \tilde{y})} \tilde{\tilde{u}}_{jk}^G(p_1, p_2, z^{(n)}; \tilde{z}). \end{aligned} \tag{35}$$

In general, the last integrand in Eq. (35) decays rapidly as a function of slowness p_2. However, when the vertical source co-ordinate $z^{(q)}$ is located at or in the neighbourhood of the observer point $z^{(n)}$, a slow decay occurs as a function of p_2 and, thus, computation of the integral can be very time-consuming. In order to improve the numerical performance, the Green's tensor $\tilde{\tilde{u}}^G_{jk}$, occuring in Eq. (35), is investigated in more detail here. The Green's tensor for the layered elastic medium can be approximated by the Green's tensor for the unbounded homogeneous medium when the observation point is close to the source. Therefore, Eq. (35) can be rewritten as

$$\begin{aligned} G^{(mn,pq)}_{jk} = {} & \delta_{jk}\delta_{pm}\delta_{nq} - \int_{y^{(p)-}}^{y^{(p)+}} \mathrm{d}\tilde{y} \int_{z^{(q)-}}^{z^{(q)+}} \mathrm{d}\tilde{z}\Delta\rho(\tilde{y},\tilde{z})\omega^2 \\ & \times \frac{\omega}{2\pi}\int_{p_2} \mathrm{d}p_2 \mathrm{e}^{\,\mathrm{j}\omega p_2(y^{(m)}-\tilde{y})}[\tilde{\tilde{u}}^G_{jk}(p_1,p_2,z^{(n)};\tilde{z}) - \tilde{\tilde{g}}_{jk}(p_1,p_2,z^{(n)};\tilde{z})] \\ & - \int_{y^{(p)-}}^{y^{(p)+}} \mathrm{d}\tilde{y} \int_{z^{(q)-}}^{z^{(q)+}} \mathrm{d}\tilde{z}\Delta\rho(\tilde{y},\tilde{z})\omega^2[\tilde{g}_{jk}(p_1,y^{(m)}-\tilde{y},z^{(n)};\tilde{z})], \end{aligned} \tag{36}$$

where $\tilde{\tilde{g}}_{ik}$ is the Green's tensor for the unbounded homogeneous medium in the slowness domain, and tensor $\tilde{g}_{jk}$ is the Green's tensor for the unbounded homogeneous medium in the (p_1, y, z)-domain. The relation between the two tensors is given by

$$\tilde{g}_{ik}(p_1,y^{(m)}-\tilde{y},z^{(n)};\tilde{z}) = \frac{\omega}{2\pi}\int_{p_2} \mathrm{d}p_2 \mathrm{e}^{\,\mathrm{j}\omega p_2(y^{(m)}-\tilde{y})}\tilde{\tilde{g}}_{jk}(p_1,p_2,z^{(n)};\tilde{z}). \tag{37}$$

For the Green's tensor of the unbounded homogenous medium in both the slowness and spatial domain, analytical expressions can be found, which are given in Appendix B.

By subtracting the tensor for the unbounded homogeneous medium $\tilde{\tilde{g}}_{ik}$, the tail of the tensor $\tilde{\tilde{u}}^G_{jk}$, in terms of p_2, is removed analytically. Consequently, long numerical computations are avoided for this term. The computation of the last term in Eq. (36) can be performed analytically after a small modification of the integration area. This is explained in the second part of the paragraph following Eq. (41). Fig. 2 serves as an illustration that the Green's tensor for the layered half-space can be approximated by the Green's tensor of the unbounded homogenous medium. In Fig. 2a, the Green's tensor elements $\tilde{\tilde{u}}^G_{33}$ and $\tilde{\tilde{g}}_{33}$ are plotted and in Fig. 2b, the difference is shown in detail, where a fast decay is observed. Subsequently, the inverse slowness transform with respect to the y co-ordinate has to be performed which is computed numerically.

By assuming that the density of the embankment is piecewise constant, and interchanging the integration order of the spatial integration and the inverse-slowness transformation, Eq. (36) can be rewritten as

$$\begin{aligned} G^{(mn,pq)}_{jk} = {} & \delta_{jk}\delta_{pm}\delta_{nq} - \Delta\rho^{(pq)}\omega^2\left[\frac{\omega}{2\pi}\int_{p_2} \mathrm{d}p_2 \int_{y^{(p)-}}^{y^{(p)+}} \mathrm{d}\tilde{y}\mathrm{e}^{\,\mathrm{j}\omega p_2(y^{(m)}-\tilde{y})}\right. \\ & \times \int_{z^{(q)-}}^{z^{(q)+}} \mathrm{d}\tilde{z}(\tilde{\tilde{u}}^G_{jk}(p_1,p_2,z^{(n)};\tilde{z}) - \tilde{\tilde{g}}_{jk}(p_1,p_2,z^{(n)};\tilde{z}))\delta^2 \\ & \left. + \int_{y^{(p)-}}^{y^{(p)+}} \mathrm{d}\tilde{y} \int_{z^{(q)-}}^{z^{(q)+}} \mathrm{d}\tilde{z}\tilde{g}_{jk}(p_1,y^{(m)}-\tilde{y},z^{(n)};\tilde{z})\right], \end{aligned} \tag{38}$$

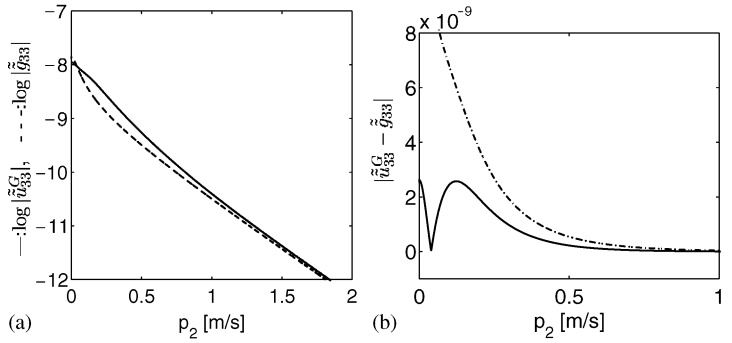

Fig. 2. (a) Green's tensor element as a function of slowness p_2 ($p_1 = 0.0440$ s/m, $z = 0.25$ m, and $z' = 0.75$ m). The solid line denotes the Green's tensor for a stratified half-space and the dashed line denotes the equivalent element for an unbounded homogeneous space. (b) Difference between the same tensor elements on a linear scale (solid line) and the Green's tensor for the stratified medium (dashed).

where $\Delta\rho^{(pq)}$ is the density contrast in grid point $(y^{(p)}, z^{(q)})$. The integration over the $\tilde{z}$ co-ordinate in the first integral on the right-hand side of Eq. (38) can be performed using the midpoint rule. The integration over the interval $\tilde{y}$ can be performed analytically. The result reads

$$G_{jk}^{(mn,pq)} = \delta_{jk}\delta_{pm}\delta_{nq} - \Delta\rho^{(pq)}\omega^2\left[\frac{\omega}{2\pi}\int_{p_2} \mathrm{d}p_2 \frac{\sin(\omega p_2\delta/2)}{\omega p_2\delta/2} \times(\tilde{\tilde{u}}_{jk}^{G}(p_1,p_2,z^{(n)};z^{(q)}) - \tilde{\tilde{g}}_{jk}(p_1,p_2,z^{(n)};z^{(q)}))\delta^2 + \int_{y^{(p)-}}^{y^{(p)+}} \mathrm{d}\tilde{y}\int_{z^{(q)-}}^{z^{(q)+}} \mathrm{d}\tilde{z}\,\tilde{g}_{jk}(p_1, y^{(m)} - \tilde{y}, z^{(n)};\tilde{z})\right]. \tag{39}$$

Regarding the second integral on the right-hand side of Eq. (39), the integration of $\tilde{g}_{jk}$ over the square area cannot be performed analytically in a straightforward manner. This is illustrated for the integration of tensor element $\tilde{g}_{11}$; a similar procedure can be applied for the other tensor elements. For this element, the second integral on the right-hand side of Eq. (39) becomes

$$\int_{y^{(p)-}}^{y^{(p)+}} \mathrm{d}\tilde{y}\int_{z^{(q)-}}^{z^{(q)+}} \mathrm{d}\tilde{z}\,\tilde{g}_{11}(p_1, y^{(m)} - \tilde{y}, z^{(n)};\tilde{z}) = \int_{y^{(p)-}}^{y^{(p)+}} \mathrm{d}\tilde{y}\int_{z^{(q)-}}^{z^{(q)+}} \mathrm{d}\tilde{z}\left[\frac{1}{\beta^2}\tilde{G}_\beta(p_1, y^{(m)} - \tilde{y}, z^{(n)};\tilde{z}) + p_1^2(\tilde{G}_\alpha(p_1, y^{(m)} - \tilde{y}, z^{(n)};\tilde{z}) - \tilde{G}_\beta(p_1, y^{(m)} - \tilde{y}, z^{(n)};\tilde{z}))\right], \tag{40}$$

with

$$\tilde{G}_\alpha(p_1, y, z;\tilde{z}) = \frac{\mathrm{j}}{4}\mathrm{H}_0^{(1)}(\omega\tilde{q}_\alpha r) \quad \text{and} \quad \tilde{G}_\beta(p_1, y, z;\tilde{z}) = \frac{\mathrm{j}}{4}\mathrm{H}_0^{(1)}(\omega\tilde{q}_\beta r), \tag{41}$$

where $\tilde{q}_\alpha = \sqrt{1/\alpha^2 - p_1^2}$ and $\tilde{q}_\beta = \sqrt{1/\beta^2 - p_1^2}$ and $r = \sqrt{y^2 + (z - \tilde{z})^2}$. Thus, the Green's tensor element consists of zeroth-order Hankel functions of the first kind. For this type of function, the two integrals can be evaluated numerically, but these calculations may be very lengthly. When performing the numerical integration, it is also necessary to account for the singularities. These singularities exist when the observation point is in the centre of the cell over which the integration is performed (i.e., when $m = p$ and $n = q$ in Eq. (40)). For square regions of integration, no closed form relations for the integrals are known. This problem can be avoided, by substituting the square area by a circular one which occupies an area of the same size. For this type of area, the closed form solution of a Hankel function over a domain integration reads

$$\int_0^{2\pi} \int_0^{\delta/\sqrt{\pi}} \frac{\mathrm{j}}{4} \mathrm{H}_0^{(1)}(\omega\tilde{q}R^{(mn)}) r^{(pq)} \mathrm{d}r^{(pq)} \mathrm{d}\theta = \frac{\mathrm{j}}{2(\omega\tilde{q})^2} \begin{cases} \sqrt{\pi}\omega\tilde{q}\delta \mathrm{H}_1^{(1)}(\omega\tilde{q}\delta/\sqrt{\pi}) + 2j & \text{if } m = p \text{ and } n = q, \\ \sqrt{\pi}\omega\tilde{q}\delta \mathrm{J}_1(\omega\tilde{q}\delta/\sqrt{\pi}) \mathrm{H}_0^{(1)}(\omega\tilde{q}R^{(mnpq)}) & \text{otherwise,} \end{cases} \tag{42}$$

where $R^{(mn)} = \sqrt{(\tilde{y} - y^{(m)})^2 + (\tilde{z} - z^{(n)})^2}$ and $r^{(pq)} = \sqrt{(\tilde{y} - y^{(p)})^2 + (\tilde{z} - z^{(q)})^2}$ and θ is the polar co-ordinate based on a co-ordinate origin at the centre of cell. The distance between the two centre point of the cells $(y^{(m)}, z^{(n)})$ and $(y^{(p)}, z^{(q)})$ is denoted by $R^{(mnpq)} = \sqrt{(y^{(m)} - y^{(p)})^2 + (z^{(n)} - z^{(q)})^2}$. For further details, the reader is referred to Richmond [9] or Zwamborn and Van den Berg [10].

In this case, the matrix elements on the left-hand side of Eq. (32) can be computed. It remains to compute the right-hand side of the equation, which follows from direct integration:

$$c_j^{(mn)} = \int \int_{y',z'} \mathrm{d}y' \mathrm{d}z' \xi^{(m)}(y') \xi^{(n)}(z') \tilde{u}_j^{inc}(p_1, y', z') \tag{43}$$

$$= \tilde{u}_j^{inc}(p_1, y^{(m)}, z^{(n)}). \tag{44}$$

Finally, the expansion coefficients $a_k^{(pq)}$ can be calculated by solving the linear system of equations (32). Once these coefficients have been obtained, the displacements in the embankment can be obtained from Eq. (29), and thus the total wave field in an arbitrary point can be constructed by computing the displacement in the slowness domain via Eq. (27) and then in the spatial domain via Eq. (10), followed by a computation of the total field with the aid of Eq. (6). The response in the time domain is obtained after inverse Fourier transformation of the result.

3. Results

Numerical computations have been performed to investigate the influence of the density contrast in the embankment on the vibration level and they have been compared with experimental data from a field experiment. Three receiver lines were laid out, two parallel to the track (one located at the rail embankment and one far from it) and one perpendicular to it. In Fig. 3, the cross-section of the geometry at the test site is shown. The rail pads lie over a rectangular embankment, the width of which is about 30 m and the height about 2 m. Parallel to the track, at a distance of about 15 m, a small filled ditch is located with a width of about 2 m.

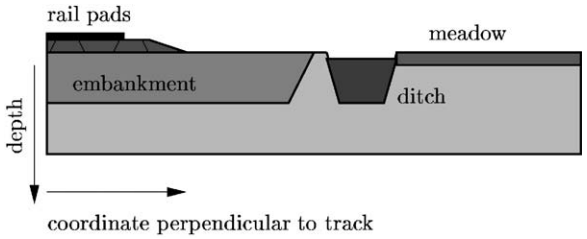

Fig. 3. Cross-section of the geometry at the test site. The rail pads lie over an embankment. At the side of the embankment, a small ditch is located.

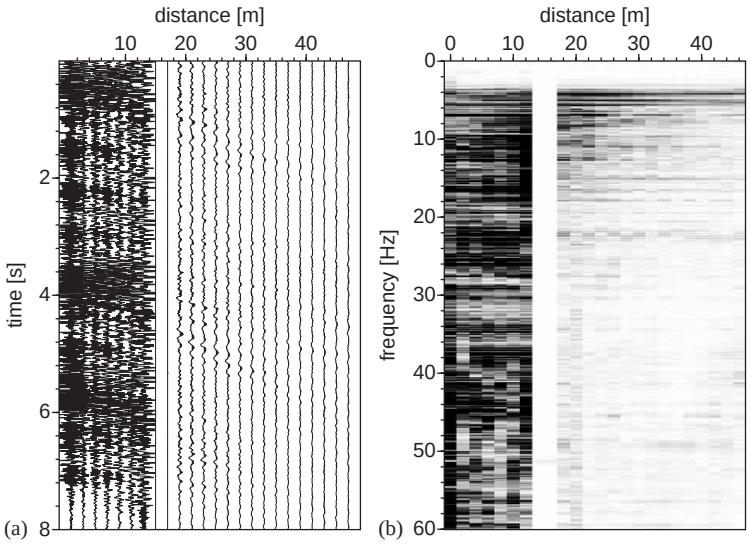

Fig. 4. Seismogram of the particle velocity (a) and its frequency spectrum. (a) Shows the vertical velocity recorded by the perpendicular line, with the zero traces showing the location of the ditch. A strong decay of higher frequencies is observed across the ditch. (b) Also shows this effect; in the embedding medium, low-frequency waves are dominant.

In Fig. 4a, a seismogram of a train passage, recorded by the perpendicular line, is displayed. In the seismogram, vertical velocity has been displayed as a function of time and distance.

Some interesting features can be observed in these data. First, in the embankment, it is observed that waves contain much higher frequencies than in the meadow. This can also be seen in Fig. 4b, where the frequency spectrum of the data has been displayed. This can be observed more clearly in the frequency spectra of two separate traces, displayed in Fig. 5a and b. Fig. 5a shows the spectrum of a trace, recorded by a receiver that is located on the embankment. Fig. 5b shows the spectrum of one trace in the meadow. One can clearly see that the dominant frequencies of the waves in the embankment lie at about 25 and 45 Hz, while the dominant frequencies in the meadow are between 2 and 15 Hz. This phenomenon can be explained by the presence of the ditch, which seems to behave as a low-pass filter. It also seems that the embankment behaves like a waveguide; waves, and especially waves containing high frequencies, are reflected by the side of

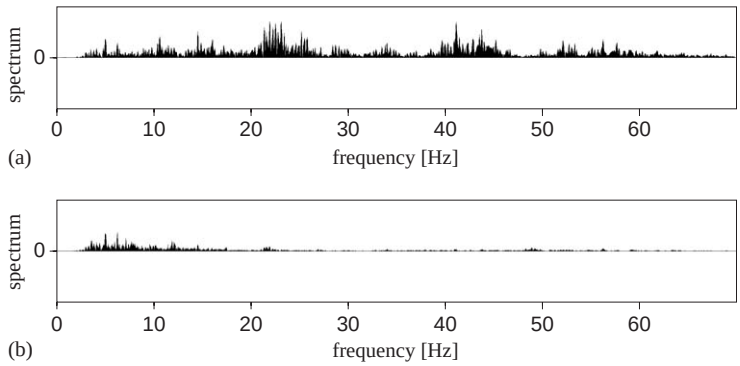

Fig. 5. Frequency spectrum of the recorded signal: (a) in the embankment at a distance of 3 m from the track, (b) in the meadow at a distance of 19 m from the track. Both figures are displayed on the same scale. In the embankment, high frequencies are dominant. One can observe that for low frequencies the spectrum is similar to the spectrum in (a). The conclusion can be drawn that for low frequencies, waves are not attenuated by the ditch.

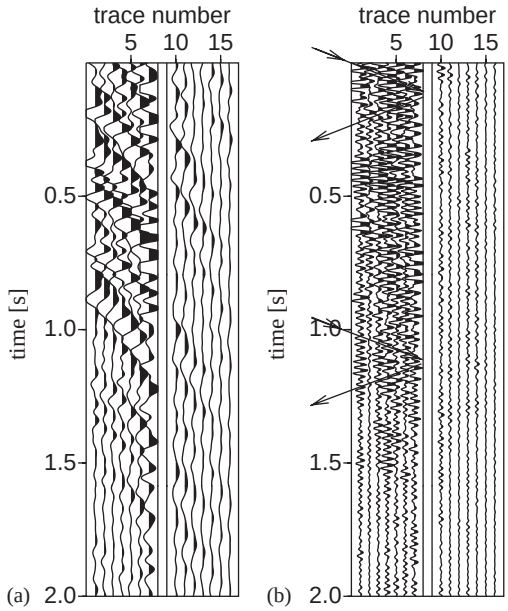

Fig. 6. Detail of response of the embankment. In (a), the low-pass filtered experimental data has been displayed, in (b) the high-pass filtered data. One can observe that especially the high-frequency waves are reflected from the boundary of the embankment. Reflected waves are indicated by arrows pointing to the left.

the embankment and are trapped in the embankment (see both Fig. 4a and b). This feature can be observed even more clearly in Fig. 6, where the low-pass filtered data (Fig. 6a) and the high-pass filtered data (Fig. 6b) are shown. Due to this 'waveguiding' behaviour a strong vibration pattern of high-frequency waves can be observed in the embankment.

These experimental results were computed with the modelled ones. First, an assumption on the near-surface model has to be made. The medium, surrounding the embankment, has been modelled by a single layer situated on top of a homogeneous substratum. The top layer is assumed to be about 9 m deep and the soil parameters have been chosen such that the shear wave travels with a speed of 60 m/s and the compressional wave with a speed of 325 m/s. The density is taken to be 1800 kg/m^3. In the substratum, the wave speeds are 380 and 1650 m/s for the shear and compressional waves, respectively. Here, the density is taken to be 2000 kg/m^3. The damping in both media is about 5%. These values are considered to be characteristic for typical Dutch soil conditions, and match the conditions of the location of this experiment and an earlier performed experiment (see Ref. [6]).

In general, a rail embankment can be characterized by its two wave speeds. In an embankment consisting of sand, the compressional wave travels with a speed of about 400–600 m/s and the shear wave with a speed of about 100–150 m/s. Generally, these wave speeds are determined by three variables, namely by the mass density and two Lamé parameters. In our case, the Lamé parameters of the embankment are equal to the ones in the top layer, and cannot be varied. Hence, proper estimates for both wave speeds can only be obtained by tuning the mass density of the embankment in the model, which will be difficult in general as the ratio between shear and compressional wave speeds varies for different soils. Therefore, another criterion than a match between the wave speeds of the actual embankment and the modelled one is employed here, namely the 'waveguiding' behaviour of the embankment. It has been shown that the embankment behaves as a waveguide, which can only be achieved in our modelling if the wave speeds in the embankment are assumed to be lower than in the embedding medium. Consequently, for the characterization of the embankment, its density has to be chosen to be higher than the density of its surroundings. In the model, the shear wave speed of the embankment is about 30 m/s and the

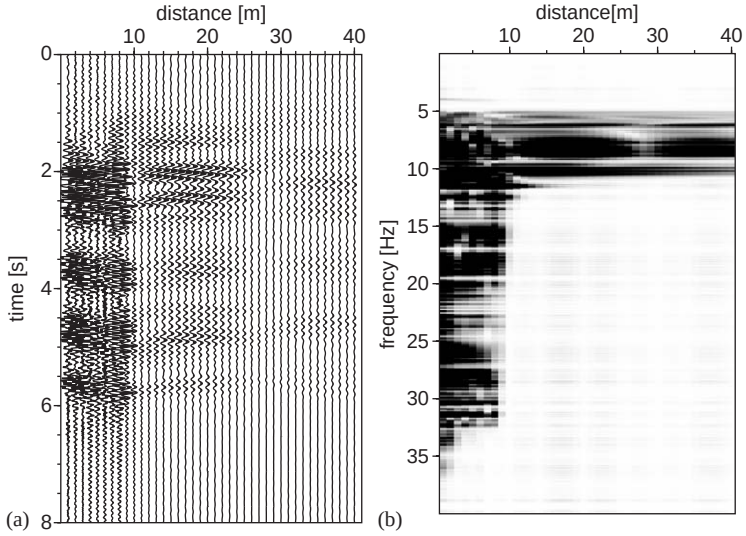

Fig. 7. Seismograms of the modelled particle velocity from a oscillating source ($\omega_c = 6.3 \cdot 2\pi$) moving at a speed of 25 m/s (see also Ref. [6]). (a) Shows the vertical velocity in the perpendicular line. A strong decay of higher frequencies is observed across the boundary of the embankment. (b) Shows the frequency spectrum of the data.

compressional wave speed is about 162.5 m/s (both being relatively slow). The embankment is modelled by a rectangular geometry, having a width of 16 m and a depth of 2 m.

In Fig. 7, the simulated response is shown; Fig. 7a shows vertical velocity as a function of time and distance perpendicular to the track. Clearly, some differences can be observed between the simulated and the experimental response (see Fig. 4), but some qualitative similarities can be observed too.

To start with the last: in Fig. 7a, one can see the surface waves travel with equal wave speeds as in the seismogram of Fig. 4a. Similar wave patterns can be observed and the arrival of different carriages can be seen. It is also seen that the waves in the embankment show a larger amplitude than in the meadow. Moreover, reflections from the boundary of the embankment are visible, especially for the high-frequency waves. In the meadow, the waves mainly contain low frequencies, similar to those observed in the experimental data. This can be observed even more clearly in Fig. 7b, where the frequency spectrum of the velocity field has been displayed. Thus, in both the modelled data and the experimental results, the 'waveguiding' behaviour of the embankment can be observed. Overall, the modelled data show a reasonable, qualitative agreement with the experimental data.

Since a qualitative agreement has been observed, the modelled results can now be investigated more closely, which might provide some qualitative insight into the effect of a rail embankment. In Fig. 8a, a surface display of the total wave field (sum of scattered and incident field) at one instant of time as a function of the horizontal co-ordinates (a snapshot) is shown. Here, the train has been modelled as a single source, oscillating with one resonance frequency of 6.3 Hz and moving at a speed of 25 m/s. This speed is slower than the slowest waves in the embedding medium and the embankment. In Fig. 8b, a snapshot of the incident wave field is shown. Both snapshots are displayed on the same scale. In Fig. 8a, one can clearly observe effects which are caused by the properties of the embankment, when comparing it to the undisturbed field in Fig. 8b. Inside the embankment, the wave field contains higher frequencies and in the embedding medium, mainly low-frequency waves are noticeable. Moreover, it can be observed that at large

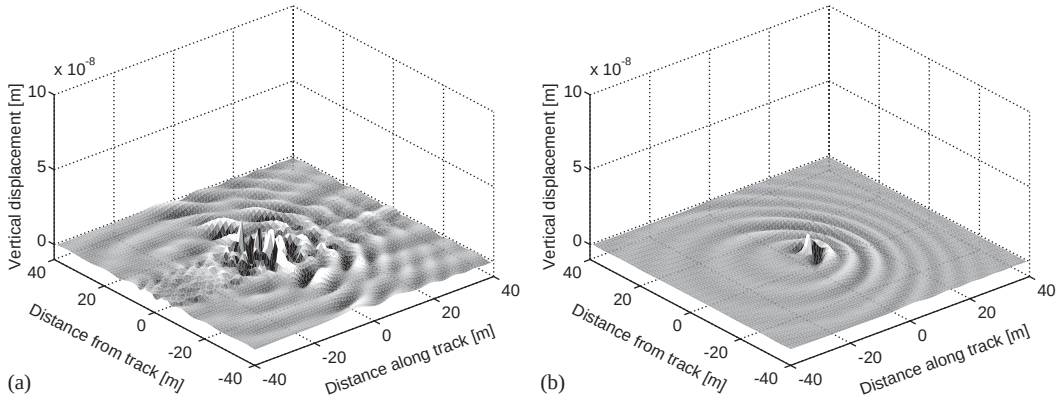

Fig. 8. Surface display of the modelled vertical displacements at one instant of time as a function of the horizontal co-ordinates (snapshot) for a train (single source) moving at a speed of 25 m/s (sub-critical). In (a), the total field has been displayed, in (b), the incident field is shown. Both figures are displayed on the same scale.

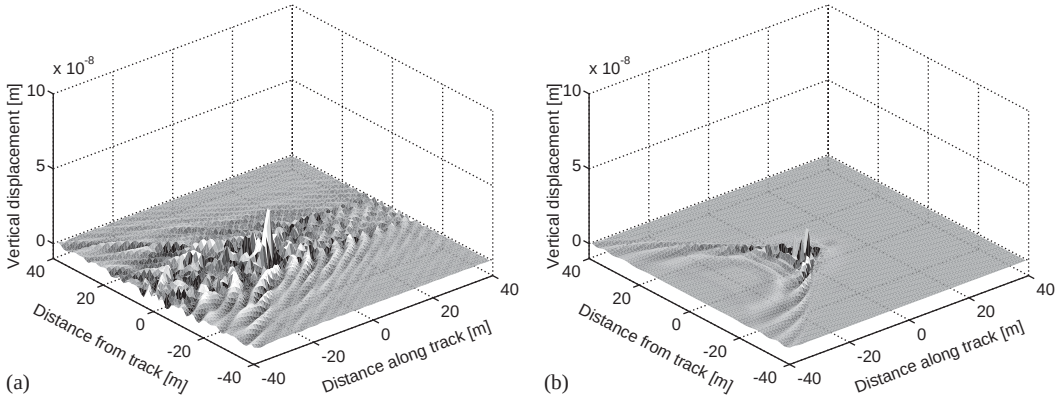

Fig. 9. Snapshot of the modelled vertical displacements for a train (single source) moving at a speed of 75 m/s. This train speed is higher than the speed of the Rayleigh wave in the surrounding medium and the embankment. In (a), the total field has been displayed and in (b), the incident field is shown. One can see the effect of the rail embankment. The cone-shape wave propagation behaviour is due to the super-critical speed of the source. Scales are similar to the scales in Fig. 8.

distances from the source, the vibrations are more pronounced now. In both Figures, one observes waves propagating forward, ahead of the train, and waves propagating backward, behind the train. It is clearly seen that waves propagating forward are more compressed than the waves propagating backward, which is due to the well-known Doppler shift. The snapshot displayed in Fig. 8a is comparable to the snapshot of the total wave field in Ref. [11, p. 280, Fig. 9.15], where Krylov discusses the influence of an embankment and has accounted for its inner reflections of an embankment by using a specific Green's function for elastic media with an embankment in his model. The differences are mainly caused by the difference in resonance frequency, but the qualitative agreement between the different methods is clear.

In Fig. 9a, a snapshot of the total wave field is shown, this time for a train running at a speed of 75 m/s, being faster than the shear wave speeds in both the top layer of the embedding medium and the embedding. In Fig. 9b, the incident wave field is shown. Again, the scales of both figures are the same, and similar to the scales in Fig. 8. Due to the super-critical speed of the train, one can clearly observe the cone-shaped profile of waves propagating away from the track behind the source like a shock wave. Here, the effect of the rail embankment on the vibration level in the surrounding soil can also be clearly seen. The snapshot displayed in Fig. 9a is comparable to the snapshot of the total wave field in Ref. [11, p. 280, Fig. 9.16].

The conclusion can be drawn that with a density contrast the waveguiding behaviour of an embankment can be modelled in a qualitative way. Although the results show a good agreement, modelling the velocity contrasts only by means of a density contrast is in some sense in contradiction with one's concept of reality, since the densities can have surrealistic values. Moreover, with a mass density contrast, the ratio between *P*-waves and *S*-waves cannot be varied, which is required when modelling a ditch. In water this ratio tends to infinity. In order to be able to vary the ratio between compressional and shear waves, which enables us to model ditch-like geometries for example, the model has to be extended to take the contrasts in Lamé parameters into account.

4. Conclusions

In this paper, an experimental and theoretical analysis is presented of the effect of a rail embankment on the vibrations generated by moving trains. The theoretical results are obtained for embankments with a density contrast relative to a layered embedding medium. The scattered field is computed from a domain-type integral equation which is solved using the method of moments. The calculations can be performed efficiently using a slowness-domain method.

It is concluded that the modelled results show a qualitative agreement with the experimental results. In both measured and modelled data, internal reflections of surface waves in the embankment can be observed, especially of the high-frequency waves.

Taking into account a contrast in Lamé parameters is necessary to vary the ratio between the compressional and shear wave speeds. Therefore, the next step would be the introduction of contrasts in Lamé parameters in the embankment, as a difference between the shear moduli of the embankment and the embedding medium is assumed to be of great importance for the vibration level. This scattering problem can be formulated in terms of a boundary-type integral equation, which is currently under investigation.

Acknowledgements

The authors would like to thank Guy Drijkoningen for conducting the experiment and bringing it to a successful end. Wybo Gardien, Herke Stuit and Francis Drossaert of Holland RailConsult are acknowledged for their help in the experiment. Furthermore, Albèr Hemstede, Martijn Frijlink and Xander Campman of Delft University of Technology are thanked for their assistance. Moreover, the help of Henk van der Meer of Utrecht University, for making available one of their recording devices, is greatly appreciated. Ranajit Ghose is acknowledged for his help in post-processing the experimental data. Peter van den Berg of Delft University is thanked for providing useful references concerning the integration of the Green's tensors.

Furthermore, the authors would like to thank two anonymous reviewers for providing constructive comments which helped to improve the manuscript.

Appendix A. Derivation of the domain-integral representation for a moving source

In this Appendix, the domain-integral representation for a source moving over an embankment with a density contrast is derived. The starting point for this derivation is the integral representation for a stationary point source, which is given in Eq. (23). It can be rewritten as

$$\bar{u}_j(x,y,z) = \bar{u}_j^{inc}(x,y,z) + \omega^2 \int_D \mathrm{d}V(\mathbf{x}')(\rho(y',z') - \rho_n)\bar{u}_{jk}^G(x,y,z;x',y',z')\bar{u}_k(x',y',z'). \tag{A.1}$$

The wave field for a moving source is now obtained by performing a superposition of wave fields due to a non-moving source, having appropriate phases (see Eq. (8))

$$\frac{1}{c}\int_{x_s} \mathrm{d}x_s \mathrm{e}^{\mathrm{j}\omega p_1^{\pm} x_s} \bar{u}_j(x-x_s,y,z) = \frac{1}{c}\int_{x_s} \mathrm{d}x_s \mathrm{e}^{\mathrm{j}\omega p_1^{\pm} x_s} \bar{u}_j^{inc}(x-x_s,y,z) + \frac{1}{c}\int_{x_s} \mathrm{d}x_s \mathrm{e}^{\mathrm{j}\omega p_1^{\pm} x_s} \int_D \mathrm{d}V(\mathbf{x}')\Delta\rho(y',z')\omega^2 \times u_{jk}^G(x-x_s,y,z;x',y',z')\bar{u}_k(x',y',z') \tag{A.2}$$

with the mass density contrast given by $\Delta\rho(y',z') = \rho(y',z') - \rho_n$. The last equation can be written as

$$\frac{1}{c}\mathrm{e}^{\mathrm{j}\omega p_1^{\pm} x}\int_{\bar{x}} \mathrm{d}\bar{x}\mathrm{e}^{-\mathrm{j}\omega p_1^{\pm}\bar{x}} \bar{u}_j(\bar{x},y,z) = \frac{1}{c}\mathrm{e}^{\mathrm{j}\omega p_1^{\pm} x}\int_{\bar{x}} \mathrm{d}\bar{x}\mathrm{e}^{-\mathrm{j}\omega p_1^{\pm}\bar{x}} \bar{u}_j^{inc}(\bar{x},y,z) + \frac{1}{c}\mathrm{e}^{\mathrm{j}\omega p_1^{\pm} x}\int_{\bar{x}} \mathrm{d}\bar{x}\mathrm{e}^{-\mathrm{j}\omega p_1^{\pm}\bar{x}} \left\{ \int_D \mathrm{d}V(\mathbf{x}')\Delta\rho(y',z')\omega^2 \times \bar{u}_{jk}^G(\bar{x},y,z;x',y',z')\bar{u}_k(x',y',z') \right\}, \tag{A.3}$$

with $\bar{x} = x - x_s$. The last term on the right-hand side can be rewritten as

$$\int_{\bar{x}} \mathrm{d}\bar{x}\mathrm{e}^{-\mathrm{j}\omega p_1^{\pm}\bar{x}} \left\{ \int_D \mathrm{d}V(\mathbf{x}')\Delta\rho(y',z')\omega^2 \bar{u}_{jk}^G(\bar{x},y,z;x',y',z')\bar{u}_k(x',y',z') \right\} = \int_{D^{\perp}} \mathrm{d}y'\mathrm{d}z'\Delta\rho(y',z')\omega^2 \times \int_{\bar{x}} \mathrm{d}\bar{x}\mathrm{e}^{-\mathrm{j}\omega p_1^{\pm}\bar{x}} \int_{x'} \mathrm{d}x' \bar{u}_{jk}^G(\bar{x}-x',y,z;0,y',z')\bar{u}_k(x',y',z'), \tag{A.4}$$

where use has been made of the fact that the integration over the embankment is built up of an integration along the parallel co-ordinate and the perpendicular co-ordinates. Also, use is made of the shift-invariance of $\bar{u}_{jk}^G$ in the $\bar{x}$ direction. Domain $D^{\perp}$ can be seen as a cross-section of the embankment (see Fig. 1b).

The two final integrations on the right-hand side in Eq. (A.4) are a slowness transform and a convolution in space with respect to the direction along the track. It is well known that the slowness transform of a convolution in space, is a multiplication of the slowness transforms in the slowness domain. Furthermore, the integrations with respect to $\bar{x}$ in Eq. (A.3), are slowness transforms. With this in mind, the following domain-integral representation in the slowness domain is found:

$$\frac{1}{c}\mathrm{e}^{\mathrm{j}\omega p_1^{\pm} x}\tilde{u}_j(p_1,y,z) = \frac{1}{c}\mathrm{e}^{\mathrm{j}\omega p_1^{\pm} x}\tilde{u}_j^{inc}(p_1^{\pm},y,z) + \frac{1}{c}\mathrm{e}^{\mathrm{j}\omega p_1^{\pm} x}\int_{D^{\perp}} \mathrm{d}y'\mathrm{d}z'\Delta\rho(y',z')\omega^2 \times \tilde{u}_{jk}^G(p_1^{\pm},y,z;y',z')\tilde{u}_k(p_1^{\pm},y',z'). \tag{A.5}$$

Dividing the result by the exponential term and accounting for the shift invariance of the Green's tensor with respect to the y co-ordinate, the domain-integral representation for a moving

source is obtained, given in Eq. (27)

$$\tilde{u}_i(p_1^{\pm}, y, z) = \tilde{u}_i^{inc}(p_1^{\pm}, y, z) + \int_{D^{\perp}} \mathrm{d}y'\mathrm{d}z' \Delta\rho(y', z')\omega^2 \tilde{u}_{ik}^{G}(p_1^{\pm}, y - y', z; z')\tilde{u}_k(p_1^{\pm}, y', z'). \tag{A.6}$$

Appendix B. Green's tensor for the unbounded homogeneous medium

Locally, the Green's tensor for the layered medium can be approximated by the tensor for an unbounded homogeneous medium. The Green's tensor for the layered medium is needed to determine the Green's matrix elements, given by Eq. (36)

$$\begin{aligned} G_{jk}^{(mn,pq)} = {} & \delta_{jk}\delta_{pm}\delta_{nq} - \int_{y^{(p)-}}^{y^{(p)+}} \mathrm{d}\tilde{y} \int_{z^{(q)-}}^{z^{(q)+}} \mathrm{d}\tilde{z} \Delta\rho(\tilde{y}, \tilde{z})\omega^2 \\ & \times \frac{\omega}{2\pi} \int_{p_2} \mathrm{d}p_2 \mathrm{e}^{\mathrm{j}\omega p_2 (y^{(m)} - \tilde{y})} \left[\tilde{\tilde{u}}_{jk}^{G}(p_1, p_2, z^{(n)}; \tilde{z}) - \tilde{\tilde{g}}_{jk}(p_1, p_2, z^{(n)}; \tilde{z}) \right] \\ & - \int_{y^{(p)-}}^{y^{(p)+}} \mathrm{d}\tilde{y} \int_{z^{(q)-}}^{z^{(q)+}} \mathrm{d}\tilde{z} \Delta\rho(\tilde{y}, \tilde{z})\omega^2 [\tilde{g}_{jk}(p_1, y^{(m)} - \tilde{y}, z^{(n)}; \tilde{z})], \end{aligned} \tag{B.1}$$

where $\tilde{\tilde{g}}_{ik}$ is the Green's tensor for the unbounded homogeneous medium in the double-slowness domain, and tensor $\tilde{g}_{jk}$ is the equivalent of the Green's tensor for the unbounded homogeneous medium in the (p_1, y, z)-domain, where the relation between the two has been given by

$$\tilde{g}_{ik}(p_1, y^{(m)} - \tilde{y}, z^{(n)}; \tilde{z}) = \frac{\omega}{2\pi} \int_{p_2} \mathrm{d}p_2 \mathrm{e}^{\mathrm{j}\omega p_2 (y^{(m)} - \tilde{y})} \tilde{\tilde{g}}_{jk}(p_1, p_2, z^{(n)}; \tilde{z}). \tag{B.2}$$

In this Appendix, the elements of the Green's tensor for the unbounded homogeneous medium are given. First, the tensor elements $\tilde{\tilde{g}}_{jk}$ in the double-slowness domain are given. The counterparts in the single-slowness domain $\tilde{g}_{jk}$ are then given. For details on wave propagation in elastic solids and plane wave representations, the reader is referred to De Hoop [12, pp. 413–417, 474–475] and Aki and Richards [13, pp. 123–133, 194–197].

In the double-slowness domain, the symmetric Green's tensor elements for the unbounded homogeneous medium read

$$\tilde{\tilde{g}}_{11}(p_1, p_2, z; \tilde{z}) = \frac{1}{\mu} \tilde{\tilde{G}}_{\beta} + \frac{p_1^2}{\rho} (\tilde{\tilde{G}}_{\alpha} - \tilde{\tilde{G}}_{\beta}), \tag{B.3}$$

$$\tilde{\tilde{g}}_{12}(p_1, p_2, z; \tilde{z}) = \frac{p_1 p_2}{\rho} (\tilde{\tilde{G}}_{\alpha} - \tilde{\tilde{G}}_{\beta}), \tag{B.4}$$

$$\tilde{\tilde{g}}_{13}(p_1, p_2, z; \tilde{z}) = -\frac{\mathrm{j}p_1}{\rho\omega} \partial_z (\tilde{\tilde{G}}_{\alpha} - \tilde{\tilde{G}}_{\beta}), \tag{B.5}$$

$$\tilde{\tilde{g}}_{22}(p_1, p_2, z; \tilde{z}) = \frac{1}{\mu} \tilde{\tilde{G}}_{\beta} + \frac{p_2^2}{\rho} (\tilde{\tilde{G}}_{\alpha} - \tilde{\tilde{G}}_{\beta}), \tag{B.6}$$

$$\tilde{\tilde{g}}_{23}(p_1,p_2,z;\tilde{z}) = -\frac{\mathrm{j}p_2}{\rho\omega}\partial_z(\tilde{\tilde{G}}_\alpha - \tilde{\tilde{G}}_\beta), \tag{B.7}$$

$$\tilde{\tilde{g}}_{33}(p_1,p_2,z;\tilde{z}) = \frac{1}{\mu}\tilde{\tilde{G}}_\beta - \frac{1}{\rho\omega^2}\partial_z^2(\tilde{\tilde{G}}_\alpha - \tilde{\tilde{G}}_\beta) \tag{B.8}$$

with

$$\tilde{\tilde{G}}_\alpha(p_1,p_2,z;\tilde{z}) = \frac{\mathrm{e}^{\mathrm{j}\omega q_\alpha|z-\tilde{z}|}}{-2\mathrm{j}\omega q_\alpha} \quad \text{and} \quad \tilde{\tilde{G}}_\beta(p_1,p_2,z;\tilde{z}) = \frac{\mathrm{e}^{\mathrm{j}\omega q_\beta|z-\tilde{z}|}}{-2\mathrm{j}\omega q_\beta}, \tag{B.9}$$

where $q_\alpha = \sqrt{1/\alpha^2 - p_1^2 - p_2^2}$ and $q_\beta = \sqrt{1/\beta^2 - p_1^2 - p_2^2}$, with $\mathrm{Re}\{q_{\alpha,\beta}\} \geqslant 0$ and $\mathrm{Im}\{q_{\alpha,\beta}\} \geqslant 0$.

The Green's tensor for the unbounded medium in the single-slowness domain, $\tilde{g}_{jk}$, can be constructed by linear combination of zeroth-order Hankel functions of the first kind. The tensor elements read

$$\tilde{g}_{11}(p_1,y,z;\tilde{z}) = \frac{1}{\mu}\tilde{G}_\beta + \frac{p_1^2}{\rho}(\tilde{G}_\alpha - \tilde{G}_\beta), \tag{B.10}$$

$$\tilde{g}_{12}(p_1,y,z;\tilde{z}) = -\frac{\mathrm{j}p_1}{\rho\omega}\partial_y(\tilde{G}_\alpha - \tilde{G}_\beta), \tag{B.11}$$

$$\tilde{g}_{13}(p_1,y,z;\tilde{z}) = -\frac{\mathrm{j}p_1}{\rho\omega}\partial_z(\tilde{G}_\alpha - \tilde{G}_\beta), \tag{B.12}$$

$$\tilde{g}_{22}(p_1,y,z;\tilde{z}) = \frac{1}{\mu}\tilde{G}_\beta - \frac{1}{\rho\omega^2}\partial_y^2(\tilde{G}_\alpha - \tilde{G}_\beta), \tag{B.13}$$

$$\tilde{g}_{23}(p_1,y,z;\tilde{z}) = -\frac{1}{\rho\omega^2}\partial_y\partial_z(\tilde{G}_\alpha - \tilde{G}_\beta), \tag{B.14}$$

$$\tilde{g}_{33}(p_1,y,z;\tilde{z}) = \frac{1}{\mu}\tilde{G}_\beta - \frac{1}{\rho\omega^2}\partial_z^2(\tilde{G}_\alpha - \tilde{G}_\beta) \tag{B.15}$$

with

$$\tilde{G}_\alpha(p_1,y,z;\tilde{z}) = \frac{\mathrm{j}}{4}\mathrm{H}_0^{(1)}(\omega\tilde{q}_\alpha r) \quad \text{and} \quad \tilde{G}_\beta(p_1,y,z;\tilde{z}) = \frac{\mathrm{j}}{4}\mathrm{H}_0^{(1)}(\omega\tilde{q}_\beta r), \tag{B.16}$$

where $\tilde{q}_\alpha = \sqrt{1/\alpha^2 - p_1^2}$ and $\tilde{q}_\beta = \sqrt{1/\beta^2 - p_1^2}$, with $\mathrm{Re}\{\tilde{q}_{\alpha,\beta}\} \geqslant 0$ and $\mathrm{Im}\{\tilde{q}_{\alpha,\beta}\} \geqslant 0$, and $r = \sqrt{y^2 + (z-\tilde{z})^2}$.

This concludes the definition of the elements of $\tilde{\tilde{g}}_{jk}$ and $\tilde{g}_{jk}$, respectively.

References

[1] V.V. Krylov, Vibrational impact of high-speed trains. I. Effect of track dynamics, *Journal of Acoustic Society of America* 100 (1996) 3121–3134.

[2] X. Sheng, C.J.C. Jones, M. Petyt, Ground vibration generated by a harmonic load acting on a railway track, *Journal of Sound and Vibration* 225 (1999) 3–28.

[3] X. Sheng, C.J.C. Jones, M. Petyt, Ground vibration generated by a load moving along a railway track, *Journal of Sound and Vibration* 228 (1999) 129–156.
[4] A.S.J. Suiker, R. de Borst, C. Esveld, Critical behaviour of a Timoshenko beam-half plane system under a moving load, *Archives of Applied Mechanics* 68 (1998) 158–168.
[5] A.V. Metrikine, K. Popp, Vibration of a periodically supported beam on an elastic half-space, *European Journal of Mechanics A/Solids* 18 (1999) 679–701.
[6] A. Ditzel, G.C. Herman, G.G. Drijkoningen, Seismograms of moving trains: comparison of theory and measurements, *Journal of Sound and Vibration* 248 (2001) 635–652.
[7] Y.H. Pao, V. Varatharajulu, Huygen's principle. Radiation conditions, and integral formulas for the scattering of elastic waves, *Journal of Acoustic Society of America* 59 (1976) 1361–1371.
[8] T.H. Tan, Scattering of elastic waves by elastically transparent obstacles (integral-equation method), *Applied Science and Research* 31 (1975) 29–51.
[9] J.H. Richmond, Scattering by a dielectric cylinder of arbitrary cross section, *IEEE Transactions on Antennas Propagation* AP-13 (1965) 334–341.
[10] P. Zwamborn, P.M. van den Berg, A weak form of the conjugate gradient FFT method for two-dimensional TE scattering problems, *IEEE Transactions on Microwave Theory and Technology* 39 (6) (1991) 953–960.
[11] V.V. Krylov, Generation of ground vibration boom by high-speed trains, in: V.V. Krylov (Ed.), *Noise and Vibration from High-Speed Trains*, Thomas Telford Publishing, 2001.
[12] A.T. de Hoop, *Handbook of Radiation and Scattering of Waves*, Academic Press, London, 1995.
[13] K. Aki, P.G. Richards, *Quantitative Seismology, Theory and Methods*, W.H. Freeman and Company, San Fransisco, CA, 1980.